HiSST: 4th International Conference on High-Speed Vehicle Science Technology
22 -26 September 2025, Tours, France

Integration Design and Analysis of Bump Inlet Based on Forebody Shock Wave

Zheng Li[1], *Huacheng Yuan*[1], *Tianlai Gu*[2]

Abstract

The integrated configuration design of hypersonic Bump inlet requires consideration of both aerodynamic constraints generated by the aircraft forebody and strong geometric constraints within the limited space of the vehicle, while simultaneously addressing inlet flowfield shock wave system organization and aerodynamic performance. The Bump inlet design method proposed in this paper divides the integrated configuration into two parts: the Bump surface profile determined based on the forebody wave system and the internal flowpath profile based on geometric fusion. Example configuration design was conducted and validated through wind tunnel test, with design point schlieren images showing that the aircraft forebody shock wave and Bump shock wave intersect at the lip, achieving excellent integration effects. Numerical simulation further analyzed the topological structure of the main separation regions and the background shock wave systems structure within the internal flowpath. The background wave system in the internal flowpath is primarily generated by the reflection of two families of shock waves induced by lip-reflected shocks and shoulder separation-induced shocks. By controlling the lip compression angle, the number of background shock waves in the internal flowpath was effectively reduced, resulting in a 12.35% increase in total pressure recovery coefficient at the isolator outlet and a 2.82% increase in outlet Mach number.

Keywords: *Hypersonic air-breathing vehicle, Integration design, Bump Inlet, Flow characteristics*

Nomenclature

a_i - Polynomial coefficients
H – Height
L – Length
Ma – Mach number
P – Static pressure
P* - Total pressure
T – Static temperature
δ – Compression angle
φ – Mass flow coefficient
π – Static pressure ratio
σ - Total pressure recovery coefficient

1. Introduction

As one of the key components of air-breathing hypersonic vehicles, the hypersonic inlet takes the responsibility of efficiently compressing incoming flow and providing sufficient airflow stably to the combustion chamber[1–3]. With the development of hypersonic vehicles towards wider speed and higher altitude ranges, the demand for inlet design technology is increasingly growing. To match the efficient and stable operation of aircrafts, airframe/propulsion system integrated design has become crucial for achieving hypersonic flight, with aircraft forebody/inlet integrated design being particularly

[1] *Nanjing University of Aeronautics and Astronautics, Nanjing, China, hypersonicLi@nuaa.edu.cn*
[2] *China Academy of Launch Vehicle Technology, Beijing, China, gutianlai2007@163.com*

important. Aircraft forebody/inlet integration methodology focusing on refined shock wave control and flight drag reduction is currently an important research direction[4, 5].

Bump inlet demonstrates good application prospects in integrated design due to its advantages of strong geometric adaptability and high anti-backpressure capability[6], where Bump surface design can reference waverider design methods. He[7–9] proposed the osculating curved cone waverider design method based on the osculating cone theory, and further developed the design method for curved external cone waverider forebody inlet combined with streamline tracing technology, conducting wind tunnel tests on flow characteristics. Zhao[10] proposed an inverse design method that controls forebody shock wave shape through design curves and obtains geometric profiles using osculating cone theory. Wang[11] developed a two-stage waverider design method based on osculating cone design theory. Waverider design theory can be conveniently applied to bump design, and the bump profile design method adopted in this paper is developed based on the osculating cone variable Mach number waverider design method proposed by Zhao[12, 13].Under ventral intake configuration, researchers have conducted a series of studies on Bump inlet and forebody integrated design. In inlet type selection, three-dimensional inward-turning inlets are typically chosen for integrated design with Bump surfaces. He[14] proposed a novel integrated design method for curved external cone waverider and inlet by sharing baseline flow field structure and streamline tracing technology between forebody and inlet. Li [15, 16]developed an aerodynamic integrated design method for curved cone forebody with three-dimensional inward-turning inlet .To better match the inlet capture cross-section and cowl profile with vehicle forebody shock waves, Qiao[17, 18] proposed an integrated design method based on forebody shock shape. By projecting the inlet capture flow tube onto the forebody shock wave surface, with baseline flow field determine d by the compression law, and the final aerodynamic profile is obtained through streamline tracing. However, three-dimensional inward-turning inlet profiles are obtained through streamline tracing in axisymmetric baseline flow fields, making it difficult to directly adjust throat section shape and position. Therefore, this paper uses geometric transition methods for inlet compression section and isolator design.

Under engineering application, bump inlet integrated design typically needs to be conducted under strong geometric constraints, while existing design methods lack consideration of geometric constraints. This paper addresses this issue by developing a bump inlet integrated design method based on forebody shock wave systems, determining Bump shock wave shape and capture cross-section shape through forebody shock wave and flow constraints, using osculating plane streamtracing and geometric transition methods for bump surface and internal flowpath profile design respectively, and conducting wind tunnel tests to validate the rationality and correctness of the proposed method. Finally, in-depth analysis of bump inlet internal flow field is conducted through numerical simulation, exploring the main flow characteristics and background shock wave system structure of bump inlet internal flowpath.

2. Bump Inlet Integrated Design Methodology

2.1. Requirements Analysis

According to different mission requirements of hypersonic vehicles, appropriate inlet types should be reasonably selected to match the aircraft forebody. In this paper, the vehicle has "glide-cruise integrated" backgrounds. As shown in Fig 1, the vehicle has two surfaces: cruise surface and glide surface. When the vehicle is in cruise state, the cruise surface is on the lower side, and the air-breathing propulsion system operates normally to provide power for hypersonic cruising. When in glide state, the glide surface is on the lower side, the air-breathing propulsion system stops working, and the vehicle relies on the high lift-to-drag ratio provided by the waverider surface for gliding. Therefore, in inlet design, consideration need to be paid for the strong geometric constraints brought by aircraft forebody leading edge, combustion entrance position, and drag reduction requirements. In aerodynamic aspect, focus should be paid on matching the forebody shock waves generated by the cruise surface during cruise state. Bump inlet has advantages such as customizable capture shape that can flexibly adapt to different forebodies, airflow deflection toward the vehicle side that can reduce isolator offset distance, and high aerodynamic performance through boundary layer removal. Therefore, this paper selects bump inlet for subsequent research on integrated design and flow field analysis.

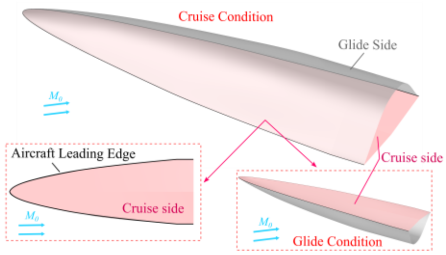

Fig 1. Aircraft layout analysis

2.2. Design Process

The bump inlet integrated configuration can be divided into bump surface profile and internal flowpath profile, where the internal flowpath includes the inlet compression surface and isolator surface. This paper introduces the bump inlet integrated configuration design method based on forebody wave systems, with the specific design process shown in Fig 2. The method's design process is mainly divided into the following 4 steps:

- (1) Determine the inlet flow capture tube (FCT) curve. Based on the selected vehicle design point flight altitude *H* and flight Mach number Ma_∞, conduct simulation calculations for the vehicle configuration and extract the forebody shock wave surface. On the basis of the forebody shock wave surface, determine the FCT curve according to flow requirements and cruise surface profile. This FCT curve is both the projection line of the inlet cowl side leading edge and the shock profile for bump surface design.
- (2) Generate bump surface profile. Using the FCT curve as the starting point for bump surface design, discretize the spatial flow field into a series of axisymmetric flow fields on two-dimensional osculating planes according to the osculating axisymmetric theory[19, 20]. Select reasonable parameters to determine the incident shock of the axisymmetric basic flow field, solve the basic flow field using the inverse method of characteristics(IMOC)[21], conduct streamline tracing within each osculating plane, and combine streamlines to obtain the complete bump surface profile.
- (3) Generate internal flowpath profile. Use a parameterized method based on cross-section control for internal flowpath profile design. Combine the inlet cowl side leading edge line and bump tail profile line as the entrance, the throat cross-section as the intermediate section, and the isolator outlet cross-section as the exit. Construct B-spline guide curves based on key cross-section positions on the symmetry plane, and finally fit the above spline curves into a B-spline tensor product surface structure to achieve smooth generation of the internal flowpath surface.
- (4) Generate integrated configuration. Combine the bump surface profile and internal flowpath profile obtained in steps (2) and (3). On this basis, perform engineering processing such as viscous correction, shoulder smoothing, and inlet leading edge blunting to obtain the complete bump inlet integrated geometric configuration.

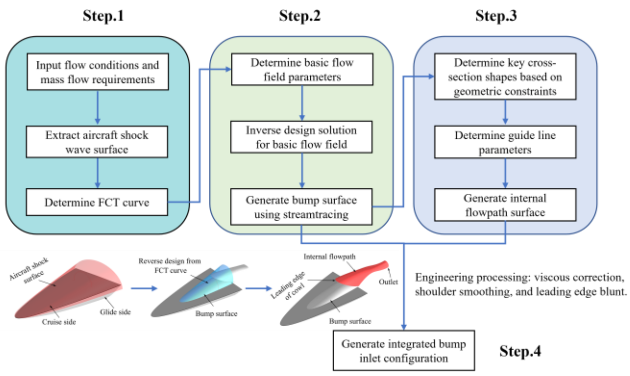

Fig 2. Flowchart of the bump inlet design method considering forebody shock

2.3. Inlet FCT Curve Design

Fig 3 shows the design principle of the FCT curve based on the forebody shock wave system. The red curve ADA' represents the forebody shock wave profile at the design flow direction position, the blue curve BDB' is the FCT curve, and the black curve CDC' represents the inlet cowl leading edge line. Point S represents the leading edge point on the aircraft symmetry plane, and point D (also known as lip point) represents the cowl point on the symmetry plane. Through numerical simulations and shock wave identification criteria[22], the forebody shock wave surface is extracted, and the forebody shock wave profile ADA' and lip point D are obtained by selecting the flow direction position. Based on flow requirements, the bump shock wave profile BDB' is determined, ensuring that the two shock wave profiles coincide at point D to achieve "shock on lip" concept. Then, within the plane passing through point D and parallel to the xOz plane, the three-dimensional lip leading edge line is designed. Point C_1 is the projection point of the cowl leading edge line within the parallel plane. Modifying the shape of curve C_1D can adjust the sweep angle of the inlet cowl.

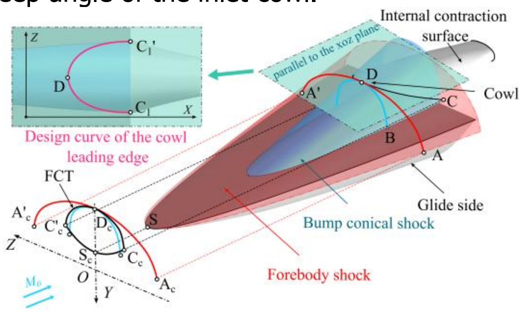

Fig 3. Design principle of the inlet FCT curve based on forebody shock wave

2.4. Bump Surface Profile Design

When designing the bump surface profile, first discretize the FCT curve and the aircraft surface profile at the same flow direction position, determine the corresponding osculating planes for each discrete point, and solve the basic flow field using the inverse method of characteristics within each osculating plane. Then, project the discrete points of the FCT curve onto the incident shock wave profile (red curve in Fig 4) within the basic flow field of each osculating plane, and use the projection point i as the starting point for streamtrace to obtain the corresponding streamlines from each osculating plane (i.e., the blue curve in Fig 4). Finally, combine the streamlines sequentially to obtain the complete bump surface profile.

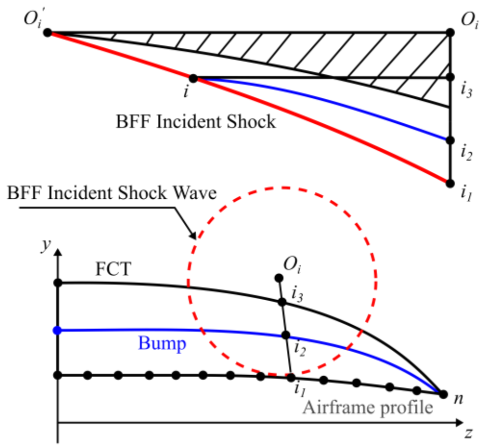

Fig 4. Bump surface profile design curves

In this paper, the incident shock wave shape of the axisymmetric basic flow field is a curved shock wave, with design parameters shown in Fig 5. Its profile equation is a cubic curve as in Eq.1

$$y = a_3x^3 + a_2x^2 + a_1x + a_0 \tag{1}$$

where a_3, a_2, a_1, a_0 are the polynomial coefficients to be determined. Here, the incident shock length-to-height ratio LH is defined as the ratio of the projection length L of the incident shock profile AB on the x-axis to its projection height H on the y-axis. The specific positions of points A and B are determined by the FCT curve and the aircraft body profile within each discrete plane. Additionally, the incident shock wave length-to-height ratio LH, and the incident shock wave starting/ending shock angles β_A and β_B need to be set. The tangent angle of the shock wave profile is the local shock angle, so by setting the incident shock wave starting/ending shock angles βA and βB, the tangent angles at points A and B can be determined. By organizing the above relationships into a system of equations and solving it, the incident shock wave profile coefficients can be determined. After obtaining the incident shock wave profile AB, it is used as the starting line for the inverse method of characteristics solution. Combining the Rankine-Hugoniot relations and the IMOC, the basic flow field can be solved.

$$\begin{cases} y_A = a_3 {x_A}^3 + a_2 {x_A}^2 + a_1 x_A + a_0 \\ tan\, \beta_A = 3a_3 {x_A}^2 + 2a_2 x_A + a_1 \\ y_B = a_3 {x_B}^3 + a_2 {x_B}^2 + a_1 x_B + a_0 \\ tan\, \beta_B = 3a_3 {x_B}^2 + 2a_2 x_B + a_1 \end{cases} \tag{2}$$

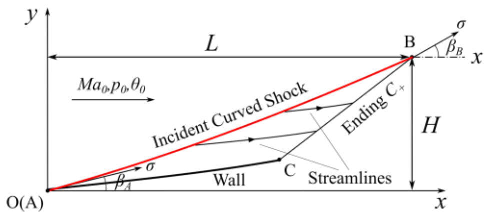

Fig 5. Curved incident shock wave and design parameters

2.5. Internal Flowpath Design

The internal flowpath of the bump inlet includes the inlet compression section and the isolator section. Due to complex shock wave system reflections and boundary layer separation within the internal flowpath, streamtracing is difficult. Moreover, the throat section and isolator outlet profile shapes and positions are required, often deviating from streamline-traced profiles. Therefore, this paper uses a geometric fusion method to generate the internal flowpath profile. As shown in Fig 6, the inlet cowl side leading edge line and the bump tail profile line are combined as the entrance, where point P_{d1} is the symmetry plane lip point (point D in Fig 3), and point P_{d2} is the symmetry plane point at the tail of the bump surface profile. The super-elliptical throat surface serves as the intermediate control section, with points P_{t1} and P_{t2} as the two endpoints of the super-ellipse minor axis. The circular isolator outlet serves as the exit, with points P_{o1} and P_{o2} as the two ends of the diameter. Referring to the B-spline surface-based internal flowpath design method proposed by Wei[23], first discretize the key cross-sections into a series of points and reconstruct them into smooth B-spline curves. Then, based on the key point positions on the symmetry plane, construct B-spline guide curves. Combined with key cross-section coordinate interpolation, calculate the intermediate cross-section coordinates, and fit them to obtain a set of intermediate cross-section B-spline curves. Finally, fit the spline guide curves and the intermediate cross-section spline set into a smooth internal flowpath profile.

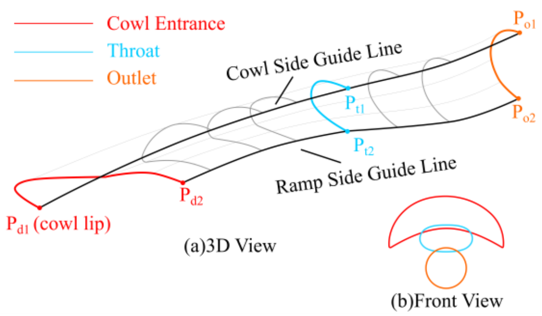

Fig 6. Parametric design principle of internal flowpath

The guide curve shape and key cross-section shape together determine the internal flowpath profile. Traditional polynomial curves as guide curves are difficult to adjust locally flexibly, so this paper selects spline curves as guide curves. As shown in Fig 7, inlet design parameters are introduced in the guide curve design, where the guide curve length and height are respectively non-dimensionalized using the internal flowpath length L and isolator outlet diameter D_{out}.The lip point, throat point on the symmetry plane, and isolator outlet point serve as guide curve control points, allowing direct adjustment of the shape and position changes of the throat cross-section and isolator cross-section. Define the tangent angle at the starting point P_{d1} of the lip side guide curve as the lip compression angle δ_c. By adjusting the lip compression angle δ_c, the strength of the lip-reflected shock wave can be adjusted.

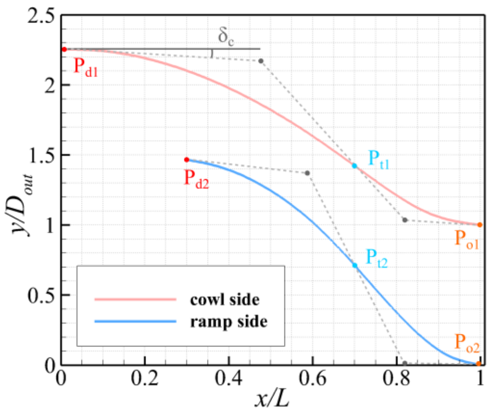

Fig 7. Parametric design principle of guide curves

3. Wind Tunnel Test Configuration Design and Numerical Methods

3.1. Bump Inlet Integrated Configuration Example

The Bump inlet integrated configuration consists of the bump surface profile, inlet compression section, and isolator section (as shown in Fig 8). The bump surface profile and inlet compression section are obtained through the aforementioned design method, and together they undertake the roles of continuously compressing airflow, adjusting airflow direction, and removing low-energy boundary layer flow. The isolator serves as a buffer section between the inlet and the combustion chamber, geometrically transitioning the inlet throat profile to the circular combustion entrance profile, and aerodynamically isolating downstream high pressure to maintain stable inlet operation. Based on the above method, example configuration design was conducted. Two configurations were designed under the same aircraft forebody and identical incoming flow conditions (Ma=6, flight altitude H=26km), named Model A and Model B. Key design parameters for the two configurations are listed in 0, where L_i is the compression section length (streamwise distance from the bump starting point to the throat cross-section on the symmetry plane), L_{iso} is the isolator length, H_{th} is the offset distance between the lip point and the throat upper point, CR is the total contraction ratio (mass capture area/throat area), ICR is the internal contraction ratio (internal compression section area/throat area), with non-dimensionalized using the isolator outlet diameter D_{out}.

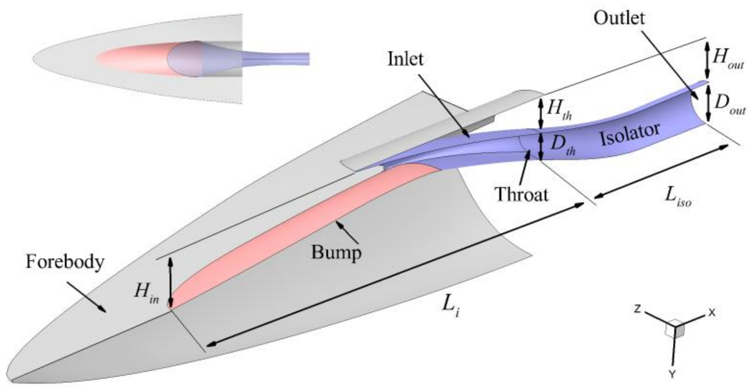

Fig 8. Bump inlet geometric configuration

Table 1. Comparison of design parameters of the two inlet

	L_i	L_{iso}	H_{th}	CR	ICR
Model A	12.238	3.497	1.301	5.096	1.984
Model B	12.238	3.497	1.231	5.096	1.897

Fig 9 compares the symmetric plane geometric profiles of the two bump inlet configurations, where the red and blue solid lines respectively correspond to Model A and Model B. Both have the same Bump surface profile, total contraction ratio, and isolator outlet shape and position. By adjusting the cowl side guide curve, the cowl compression angles are respectively set to 5° and 3° for the two configurations. Model A has a larger cowl compression angle, which increases the strength of the cowl-reflected shock.

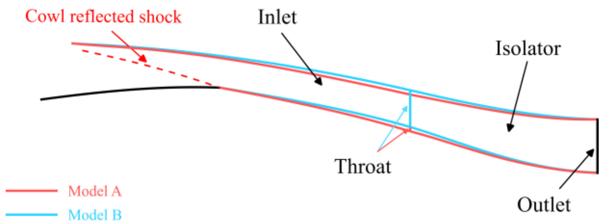

Fig 9. Figure 9. Comparison of Bump inlet symmetric plane geometric profiles

3.2. Wind Tunnel Test Conditions

To verify the correctness and effectiveness of the bump inlet integrated configuration design method based on forebody shock proposed in this paper, wind tunnel tests were conducted based on the Model B configuration. The relevant wind tunnel tests were carried out in the Φ1000mm hypersonic wind tunnel at the China Aerodynamics Research and Development Center(CARDC). This wind tunnel is a high-pressure blowdown-vacuum suction intermittent hypersonic wind tunnel with a Mach number range of 3~10, a nozzle exit diameter of 1.0m, and Mach number changes in the test section are achieved by replacing nozzles. Simultaneously, the wind tunnel is equipped with a Φ800mm schlieren system, a multi-channel electronic scanning valve pressure measurement system, and a multi-degree-of-freedom model angle of attack mechanism to meet the needs of flow field observation and data acquisition under different angle of attack conditions during the tests. The test model was installed in the wind tunnel test section as shown in Fig 10. The test model scale is 1:6, with a series of static pressure measurement points arranged along the symmetry plane in the flow direction to capture the pressure distribution along the inlet. The model tail is equipped with a circular mass flow tube and a plug system (including a throttle plug and a stepper motor control system) for accurate mass flow measurement and simulation of backpressure changes at the isolator outlet. The test Mach numbers are 5.0, 6.0, and 6.5, with specific wind tunnel inflow parameters listed in Table 2. During the tests, focus was on the through-flow performance, angle of attack characteristics, and backpressure characteristics of the inlet configuration at the design point Ma=6 to validate the rationality of the design method.

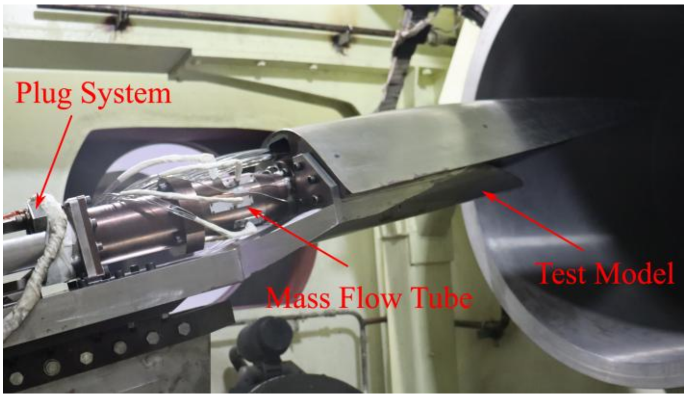

Fig 10. Model installation position in the wind tunnel test section

Table 2. Experimental parameter range of the wind tunnel

Nominal, Ma	Actual, Ma	Total temperature(K)	Total pressure(Mpa)	Unit Reynolds number(m^{-1})
5.0	4.923	407.260	1.016	9.295×10^6
6.0	6.006	486.750	2.017	8.395×10^6
6.5	6.537	553.260	2.546	7.255×10^6

3.3. Preparation of Numerical Simulation

The flow field of the bump inlet integrated configuration contains complex flow phenomena such as shock wave/boundary layer interaction, streamwise vortex development, and low-energy flow migration. Wind tunnel tests alone are insufficient to observe the detailed inlet flow field, so validated numerical calculation methods are needed to supplement the three-dimensional flow field characteristics.

In this paper, the governing equations use the Reynolds-averaged Navier-Stokes (RANS) equations, and compressible flow is solved based on finite volume implicit time advancement. Inviscid flux calculation adopts the second-order Roe-FDS upwind scheme, and the flow equations are spatially discretized using the second-order upwind scheme. The gas model uses an ideal gas with constant specific heat ratio γ=1.4, the turbulence model selects the SST k-ω model, and molecular viscosity coefficient calculation uses the Sutherland formula. During the calculation process, convergence is judged by monitoring residual change trends, key sections mass flow rates, mass-averaged Mach number and pressure. Calculation is considered converged when the residual decreases by three orders of magnitude, the difference between throat and isolator outlet mass flow rates relative to throat flow rate is less than 1%, and the mass-averaged Mach number and pressure at the throat and isolator cross-sections remain unchanged. Fig 11 shows the mesh division and boundary condition settings for the bump inlet integrated configuration simulation. Boundary conditions include pressure far field, pressure outlet, symmetry plane, and no-slip wall. Grid refinement is applied on both sides of shock wave discontinuities and in the wall normal direction to ensure accurate capture of main shock wave system structures and precise simulation of viscous flows.

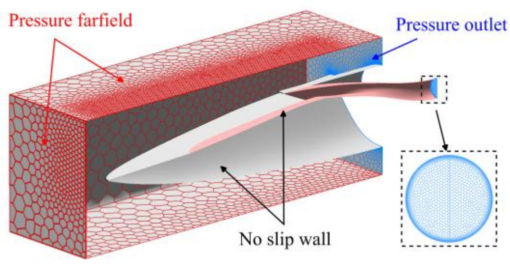

Fig 11. Numerical calculation grid and boundary conditions

As shown in Fig 12, the above numerical method is used to calculate the bump inlet integrated configuration, using the same model as the wind tunnel test model, and comparing simulation results with wind tunnel test results. The numerical calculation inflow conditions are consistent with the *Ma6* inflow conditions provided by the wind tunnel. Fig 13(a) shows the consistent bump inlet wave system structure obtained from numerical calculation and schlieren imaging. The forebody shock wave generated by the aircraft body and the incident shock wave generated by the bump surface both converge at the lip, therefore reducing lip spillage. Fig 13(b) further compares the static pressure ratio distribution along the cowl side and ramp side on the symmetry plane of the configuration. The numerical results and wind tunnel test results show good agreement, indicating that the numerical method used in this paper can accurately capture the main flow field characteristics of the inlet with high reliability.

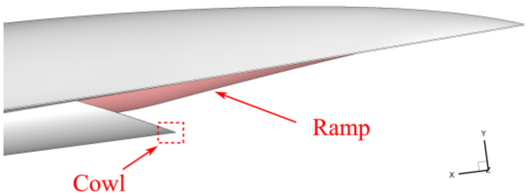

(a) Numerical calculation model

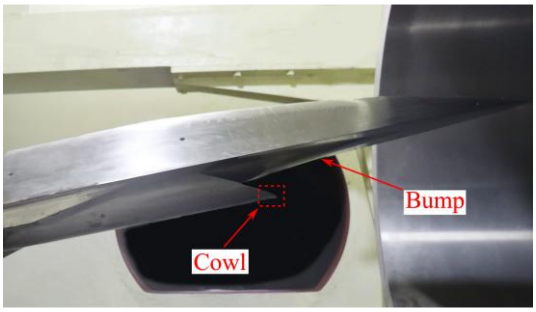

(b) Wind tunnel test model

Fig 12. Numerical validation and wind tunnel test model

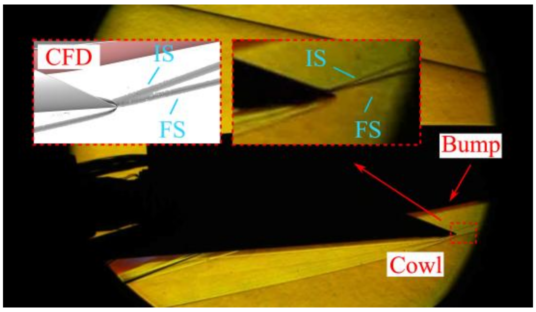

(a) Inlet compression wave system structure

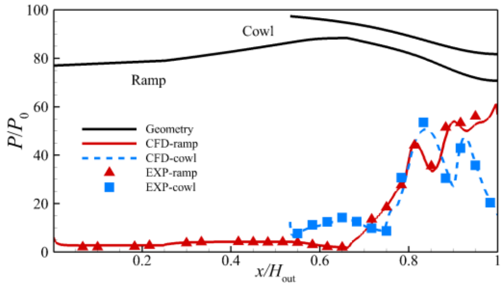

(b) Pressure distribution along cowl and ramp side of symmetry plane

Fig 13. Comparison of numerical simulation and wind tunnel test results

4. Results and Discussions

To verify the effectiveness of the bump inlet integrated configuration design method based on forebody shocks proposed in this paper, and to explore the typical shock wave system structures, separation region formation mechanisms, and low-energy flow migration characteristics under through-flow conditions, the flow field structures of Model A and Model B configurations at the design point (Ma=6, H=26km, α=6°) were analyzed and compared.

4.1. Shock Wave System Structure Analysis

Fig 14 (a) shows the Mach number contour distribution on the symmetry plane of Model A configuration, with a local magnification of the flow field near the cowl provided below the image. As can be seen, the shock wave system structure of the bump inlet compression section mainly consists of the forebody shock, bump incident shock, and cowl-reflected shock. The shapes of the forebody shock and incident shock wave are consistent with the design shock wave shapes, and both converge at the cowl. Both configurations have the same bump surface and cowl leading edge shape, so the airflow decelerates to Ma=4.70 before reaching the reflected shock wave. In Model A configuration, the cowl emits a reflected shock wave that intersects with the ramp side shoulder. The shoulder rounding treatment causes local expansion and acceleration of the airflow. After passing through the lip-reflected shock wave, the mainstream velocity decreases to Ma=3.90. Under the combined effects of increased Mach number ahead of the reflected shock wave and reflected shock wave/boundary layer interaction, a small-scale separation occurs at the ramp side shoulder of the configuration. As shown in Fig 14(b), Model B configuration has a smaller offset distance, and the compression degree on the cowl side is lower than that of Model A configuration (see Fig 9). Therefore, its cowl-reflected shock wave angle decreases, and the intersection point with the ramp side wall moves rearward. The mainstream velocity after the cowl-reflected shock wave in Model B configuration is Ma=4.05. The reduced strength of the reflected shock wave alleviates the shock wave/boundary layer interaction intensity, resulting in a significantly smaller shoulder separation region compared to Model A configuration. Overall, the shock wave system structure distribution on the symmetry plane meets expectations, and the forebody shock system and inlet shock system achieve good agreement, realizing effective integrated design and validating the effectiveness of the Bump inlet integrated design method proposed in this paper.

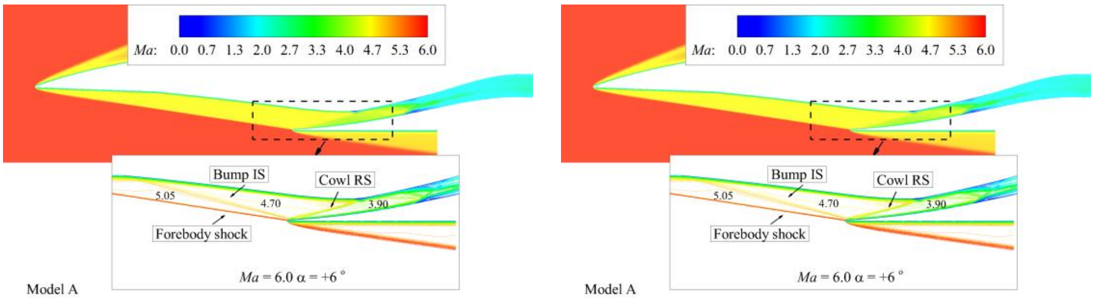

(a) Model A (b) Model B

Fig 14. Mach number contour plots on the symmetry plane of the two configurations

The flow field of the bump inlet integrated configuration exhibits significant three-dimensional characteristics. Below, the three-dimensional flow field is analyzed using Mach number iso-surfaces and spanwise cross-sections of the two configurations. As shown in Fig 15, the three-dimensional wave system structures of the forebody shock wave surface, incident shock wave surface, and reflected shock wave surface are clear and distinctly separated. The forebody shock wave surface intersects with the aircraft body on both sides before the bump surface. Near the symmetry plane, the incident shock wave surface and forebody shock wave surface converge at the lip. As they develop toward both sides of the vehicle body, the incident shock wave surface and forebody shock wave surface gradually separate. Additionally, combined with Fig 14, it can be seen that the shock wave reflections within the isolator are complex, and significant separation regions exist on both cowl and ramp walls, affecting the flow uniformity and aerodynamic performance of the inlet. Further analysis of the flow within the isolator is necessary in the following sections.

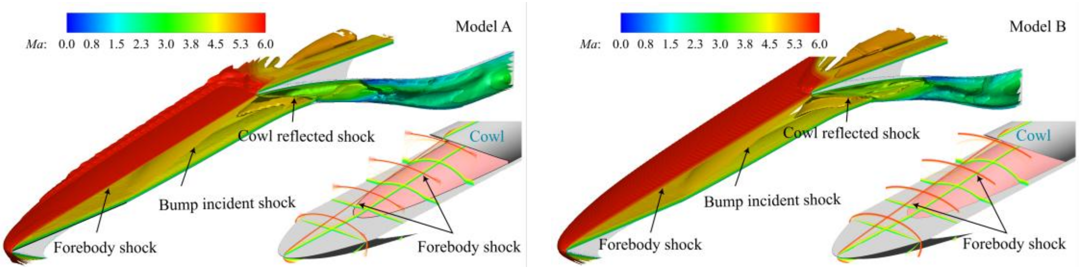

(a) Model A (b) Model B

Fig 15. Comparison of Mach number distribution iso-surfaces and spanwise Mach number distributions

4.2. Internal Flowpath Flow Analysis

As shown in Fig 14, both Model A and Model B configurations have separation regions at the shoulder and ramp side within the internal flowpath. This section will analyze the formation mechanisms of various separation regions in the bump inlet configuration. The bump inlet internal flowpath contains multiple three-dimensional separated flows. Babinsky[24] pointed out that three-dimensional flow separation exhibits two typical topological structures, as shown in Fig 16(a). The first topological structure includes two saddle points: separation saddle point S1 and reattachment saddle point S2, located at the midpoint of the separation line and reattachment line, respectively. The separation line extends along the spanwise direction toward both sides, eventually converging into a pair of focus points F. Compared to the first topological structure, the second topological structure in Fig 16(b) has slightly different critical point distribution, mainly reflected in the reattachment region: the saddle point S2 on the reattachment line becomes two and shifts toward both sides in the spanwise direction; a reattachment node N appears at the midpoint of the reattachment line. In both topological structures, the focus F correspond to tornado vortices in three-dimensional space, while the reattachment node in the second topological structure is caused by "horseshoe vortices" in space.

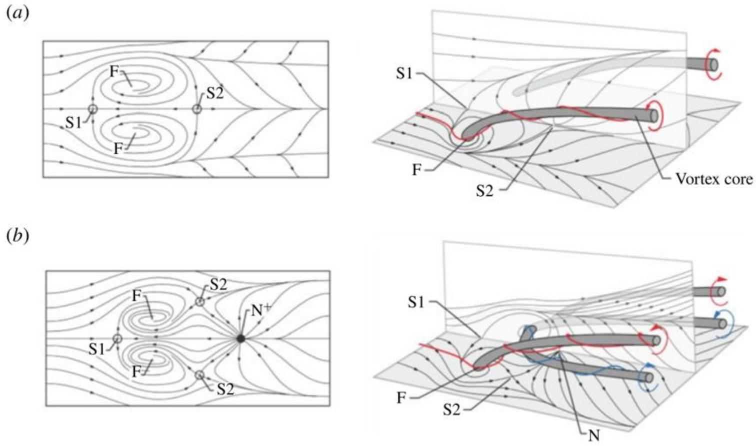

Fig 16. Two typical "owl-face" flow separation topological structures[24]

According to the wall limiting streamlines and wall static pressure ratio distribution of Model A shown in Fig 17 , focus on the flow field structures in the following four regions: 1.cowl side upper wall, 2. ramp side shoulder, 3.side wall near the throat plane, 4.corner region at the internal compression section entrance. In region 1, a series of approximately parallel streamlines are emitted from the cowl leading edge line, while the side nodes N2, N'2 on both sides are influenced by the high-pressure region generated by side wall contraction, emitting a series of streamlines converging toward the center. These two streams of streamlines converge at the centerline to form separation saddle point S1 and a pair of focus F1F'1, generating reattachment saddle point S2 downstream. The flow in this region belongs to the first topological structure in Fig 16. Region 2 has a significant shoulder separation region. The side nodes N4N'4 on the lower wall emit streamlines toward the center to form saddle point S4. The streamlines emitted upstream from saddle point S4 intersect with the incoming flow to form saddle point S3, and converge with streamlines emitted upstream from node N4 to form separation initiation line S5-S3-S'5. This separation initiation line has a saddle-point-node-saddle-point structure. The separation and reattachment lines in this region are regularly distributed, with almost identical separation region lengths along the spanwise direction, exhibiting certain two-dimensional characteristics.

At the internal compression section entrance, the compression lower wall and cowl side wall form a corner region. Both are irregular curved surfaces, and the cowl leading edge is blunted, increasing the complexity of flow in this region. Region 4 contains three main nodes: cowl side node N2, lower wall side node N4, and intersection node N6 between the lower wall and cowl. All three nodes emit streamlines in all directions, with streamlines emitted upstream forming the cowl root overflow region. Streamlines are mutually emitted between the three nodes, with node N6 converging with some streamlines emitted from nodes N2 and N4 to form saddle points S9 and S8, respectively. Some streamlines emitted downstream from nodes N2 and N6 converge with the cowl incoming flow to form the separation structure in region 1, while others develop toward the downstream side wall. Some streamlines emitted downstream from nodes N4 and N6 converge with the compression surface side incoming flow to form the shoulder separation region, while others also develop toward the downstream side wall. The two streams of limiting streamlines both developing toward the downstream side wall converge to form saddle point S7 in region 3. The limiting stream emitted upstream from saddle point S7 meets the incoming airflow to form saddle point S6, with one focus F2 and one node N5 on either side of the local flow centerline S6-S7. Since a node can be considered as an incompletely degenerated focus, the separation structure in region 3 can be regarded as a variant of the first topological structure in Fig 16.

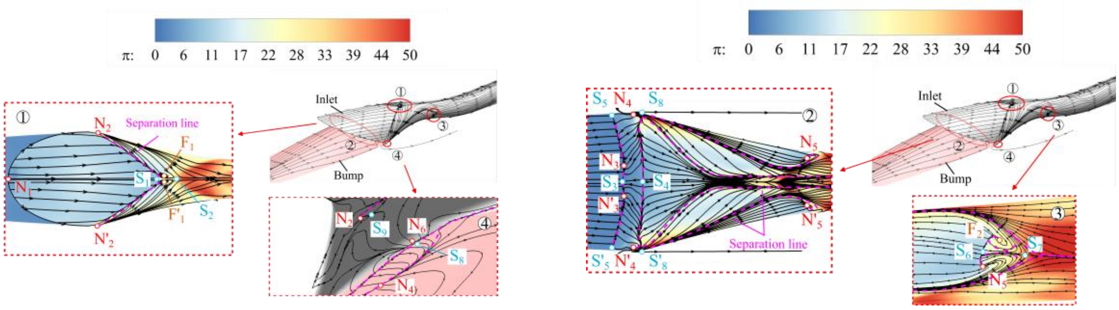

(a) Cowl side and internal compression section entrance corner region

(b)ramp wall and side wall

Fig 17. Wall limiting streamline distribution of Model A configuration

Fig 18 shows the wall limiting streamline and wall static pressure ratio distribution of Model B configuration, which has the same four separation regions as Model A configuration. The flow topological structures in regions 1 and 3 are also the first topological structure in Figure 16, forming tornado vortices. Region4 still contains three key nodes: cowl side node N2, lower wall side node N4, and intersection node N7 between the lower wall and cowl. The node-saddle-point-node structure also exists in N2-S9-N7 and N4-S8-N7. Model B configuration uses a straight swept design for the cowl root, different from the rounded design in Model A configuration. Node N2 is closer to the intersection line between the compression surface and cowl surface, while saddle point S8 and node N4 are farther from the intersection line. As shown in Fig 18(b), the separation region width in region 2 exhibits a "W" shaped distribution, different from the rectangular distribution of Model A configuration's separation region. Due to the reduced compression degree on the cowl side of Model B configuration (see Figure 9), the strength of the cowl-reflected shock wave is reduced. The separation region length significantly decreases at the symmetry plane, showing a trend of first increasing then decreasing when developing toward both sides. Overall, the shoulder separation region scale of Model B configuration is somewhat reduced.

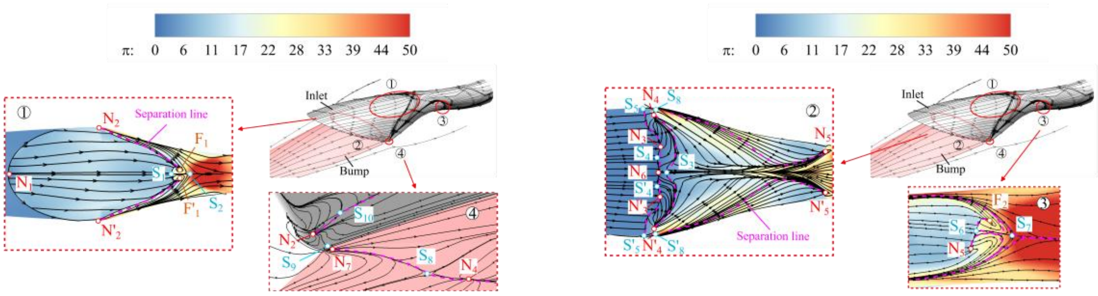

(a) Cowl side and internal compression section entrance corner region

(b)ramp wall and side wall

Fig 18. Wall limiting streamline distribution of Model B configuration

Both the ramp surface and isolator surface of the bump inlet are three-dimensional surfaces with side contraction, resulting in complex background wave systems in the internal flowpath. Therefore, it is necessary to conduct in-depth analysis of the three-dimensional background wave system structure in the internal channel, providing δ_p distribution contour plots in symmetry plane A-A and oblique cross-section B-B (specific geometric positions are shown in the lower left corner of the figure). δ_p is a variable used to characterize shock waves and expansion waves. When the value is greater than 0, it represents airflow compression regions; when less than 0, it represents airflow expansion regions. The reliability of this variable for characterizing wave systems has been verified in references[25, 26]. As shown in Fig 19(a), the external compression wave system of Model A configuration consists of the forebody shock wave and incident shock wave. The background wave system consists of the cowl-reflected shock wave and compression shock wave system CS_A, where CS_A is composed of 5 oblique shock waves. Comparing with Fig 19(b) of Model B configuration, both have external compression wave systems and cowl-reflected wave systems, but the compression wave system CS_B of Model B configuration consists of 3 oblique shock waves, differing from Model A configuration's compression wave system. From the δ_ρ distribution in oblique cross-section B-B, it can be seen that the background wave system of Model A configuration consists of swept shock waves, shoulder separation-induced shock waves, and corresponding reflected shock wave systems, while Model B configuration's background wave system only contains swept shock waves and corresponding reflected wave systems. The background wave systems all exhibit "X" shaped distributions. After reflection, the airflow Mach number decreases, subsequent shock wave strength weakens, and compression and expansion regions alternate show up.

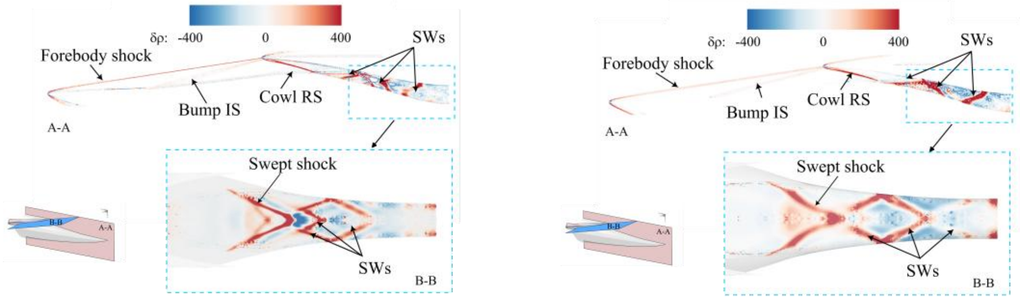

(a) Model A (b) Model B

Fig 19. δ_ρ contour distribution in typical cross-sections of the two configurations

For convenience of description, the internal flowpath is divided into three regions according to the background wave system structure, as shown in Fig 20: (1) Region starting from the cowl position, ending at the streamwise position of intersection line A1A'1 between cowl-reflected shock wave CRS and lower wall; (2) Region starting from the streamwise position of $A_1A'_1$, ending at the streamwise position of intersection line $A_3A'_3$ between the first family reflected shock wave and side wall; (3) Region starting from the streamwise position of intersection line $A_3A'_3$, ending at the streamwise position of the isolator outlet plane. Taking Model A configuration as an example for analysis, as shown in Fig 20(a), the cowl-reflected shock wave CRS is a three-dimensional shock wave emitted from the cowl side, intersecting the lower wall at $A_1A'_1$ and reflecting to produce the first family shock wave system in the internal flowpath. Simultaneously, shock wave/boundary layer interaction causes lower wall separation. The induced wave system of this separation bubble reflects back and forth in the internal flowpath, producing the second family shock wave system. In region (2), shock wave I-1 is emitted from the lower wall at $A_1A'_1$. Under the compression effect of the side wall toward the center, shock wave I-1 develops downstream while contracting toward the configuration center, intersecting the cowl side wall and inducing cowl side separation SB (see Fig 14). C1 is the starting point of separation bubble SB, and the separation-induced shock wave emitted from the cowl side intersects the lower wall at point C_2. Shock wave I-1 converges and reflects at point A_2 to produce shock wave I-2, which develops from the center toward both sides and intersects the side wall at points $A_3A'_3$. Shock wave II-1 is emitted from the lower wall at $B_1B'_1$, also converging at point B_2 under the contraction effect of the side wall. In region (3), shock wave I-3 is the reflected shock wave of shock wave I-2 emitted from the side wall, converging at point A_4 to produce shock wave I-4. Since the calculation is under through-flow conditions, there is no high backpressure at the isolator outlet, so shock wave I-4 develops from the center toward both sides and does not reflect again after intersecting the side wall. Shock wave II-2 is emitted from point B_2 and intersects the side wall at points $B_3B'_3$, reflecting to produce shock wave II-3. As shown in Fig 20(b), the first family shock wave system produced by the cowl-reflected shock wave still exists in Model B configuration, with similar intersection and reflection patterns to Model A. However, due to significantly reduced shoulder separation, the second family shock wave system is not produced, resulting in a simpler internal flowpath wave system structure. It is worth noting that both the first and second family shock wave systems are three-dimensional curved shock waves, but their intersection and reflection patterns are very similar to the regular reflection (RR) pattern of two-dimensional oblique shock waves.

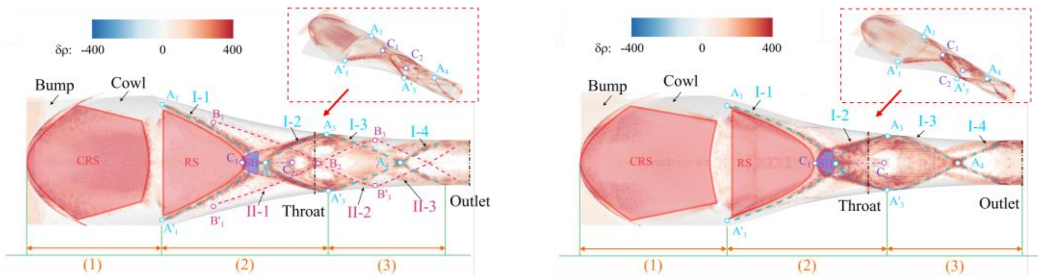

(a) Model A (b) Model B

Fig 20. Three-dimensional δ_p contour distribution of the two inlet configurations

Table 3 shows the aerodynamic performance comparison of the two inlet configurations at the design point Ma=6, H=26km, α=6° for throat section and isolator outlet, where subscript th represents throat cross-section parameters, subscript e represents outlet cross-section parameters, φ represents mass flow coefficient, $\pi=p/p_0$ represents static pressure ratio (p_0 is incoming static pressure), σ represents total pressure recovery coefficient, Ma represents Mach number, and cross-section performance parameters are obtained through mass-weighted average. According to the data in Table 3, the mass flow coefficients of the two inlet configurations are respectively 0.966 and 0.969, both achieving high mass flow capture, demonstrating the effectiveness of the bump/inlet integrated design method based on forebody shock wave systems. Model B configuration shows a 10.361% increase in total pressure recovery coefficient at the throat section, a 2.904% increase in throat Mach number, a significant 12.346% increase in total pressure recovery coefficient at the isolator outlet cross-section, and a 2.818% increase in isolator outlet Mach number. The reduced cowl compression angle of Model B configuration decreases the strength of the cowl-reflected shock wave and reduces the size of the ramp wall shoulder separation region, decreasing the number of background shock wave systems in the internal flowpath, thereby reducing aerodynamic performance, consistent with the previous analysis of flow field wave system structures.

Table 3. Comparison of aerodynamic parameters of the two inlet

	φ	π_{th}	σ_{th}	Ma_{th}	π_e	σ_e	Ma_e
Model A	0.966	35.418	0.531	2.684	30.530	0.344	2.554
Model B	0.969	36.737	0.586	2.762	29.641	0.387	2.626
Δ	0.31%	3.725%	10.361%	2.904%	-2.911%	12.346%	2.818%

5. Conclusions

Existing inlet/aircarft integrated design methods mostly adopt a positive layout of the inlet, which on one hand makes it difficult to meet the strong geometric constraints of actual aircraft, and on the other hand, the airflow compression direction deviates from the aircraft center, leading to additional flow losses. To address this issue, this paper proposes a bump inlet design method based on forebody shock waves and key cross-section control, achieving integrated design under strong geometric constraints. Based on this method, two sets of integrated bump[27] inlet configurations with different internal flowpath guide lines were designed under the same design constraints, and the rationality and correctness of the design method has been validated through wind tunnel tests. Further, numerical simulation was used to explore the main flow characteristics and background shock wave system structure within the bump inlet internal flowpath. The conclusions are as follows:

1. The Bump inlet integrated design method proposed in this paper divides the integrated configuration into three parts: Bump surface, inlet surface, and isolator section. The Bump surface is obtained through inverse solution based on forebody shock waves and mass flow requirements, while the inlet and isolator surfaces achieve a smooth transition from the bump surface to the downstream combustion chamber entrance surface through key section control. Wind tunnel tests were conducted to validate the design method and numerical methods. The results show that the design method proposed in this paper can achieve good bump/inlet aerodynamic fusion integration and rapid iteration of the internal

flowpath under strong geometric constraints; meanwhile, the numerical methods used in this paper have high reliability and can accurately simulate the complex internal flow field of the inlet.

2. There are three main separation zones in the bump inlet flowfield: ramp side shoulder separation, cowl side separation, and side wall separation. Among them, the ramp side shoulder separation is caused by the interaction between the cowl-reflected shock and the near wall boundary layer. The cowl side separation and side wall separation are caused by the interaction between the I-1 shock wave of the first family background shock wave system and the cowl side boundary layer, and the I-2 shock wave and the side wall boundary layer, respectively. The ramp side shoulder separation is a typical single incident shock wave/boundary layer interference separation, while the topological structures of the cowl side separation and side wall separation belong to the classic "owl-face" distribution.

3. The external compression section wave system of the bump inlet configuration is dominated by the forebody shock wave and bump incident shock wave. Its internal flowpath wave system results mainly consist of the cowl-reflected shock and two families of background shock wave systems. The first family shock wave system is generated by the cowl-reflected shock, and the second family shock wave system is induced by the ramp side separation bubble. By reducing the cowl compression angle, the size of the ramp side separation bubble can be effectively suppressed, eliminating the second family shock waves and reducing the number of internal flowpath shock wave, thereby effectively improving the inlet aerodynamic performance. Simulation results show that compared to Model A configuration, Model B configuration has a 10.36% increase in throat total pressure recovery coefficient, a 2.9% increase in throat Mach number, a 12.35% increase in isolator outlet total pressure recovery coefficient, and a 2.82% increase in outlet Mach number.

References

1. Liu, C., Ai, J., Zhang, J., Li, X., Zhao, Z., Huang, W.: Research progress of the flow and combustion organization for the high-Mach-number scramjet: From Mach 8 to 12. Progress in Aerospace Sciences. 101094 (2025). https://doi.org/10.1016/j.paerosci.2025.101094
2. Huang, H.-X., Tan H.-J., Zhuang Y., Sheng F.-J., Sun S.: Progress in Internal Flow Characteristics of Hypersonic Inlet/Isolator. Journal of Propulsion Technology. 2252–2273 (2017) (in Chinese). https://doi.org/10.13675/j.cnki.tjjs.2018.10.010
3. Zuo, F.-Y., Mölder, S.: Hypersonic wavecatcher intakes and variable-geometry turbine based combined cycle engines. Progress in Aerospace Sciences. 106, 108–144 (2019). https://doi.org/10.1016/j.paerosci.2019.03.001
4. Qu, F., Wang, X., Zhong, J., Qu, H.: Aerodynamic design optimization of the hypersonic inward turning inlet in wide-speed range. Physics of Fluids. 36, 127109 (2024). https://doi.org/10.1063/5.0234961
5. Qiao, W., Yu, A.: Overview on integrated design of inward-turning inlet with aircraft forebody. Journal of Experiments in Fluid Mechanics. 33, 43–59 (2019) (in Chinese). https://doi.org/10.11729/syltlx20190028
6. Zhu Y., Cheng H.-J., Chen C., Huang H.-X., Tan H.-J.: On the Mechanism of Bump inlet stable working at supersonic speed. Acta Aeronautica et Astronautica Sinica. 45, 130408–130408 (2024) (in Chinese).
7. He, X., Zhou, Z., Qin, S., Wei, F., Le, J.: Design and experimental study of a practical Osculating Inward Cone Waverider Inlet. Chinese Journal of Aeronautics. 29, 1582–1590 (2016). https://doi.org/10.1016/j.cja.2016.09.007
8. He, X., Wei, F., Liu, F., Chen, S.: Integrated design of minimal wave drag cone-derived waveriders and three-dimensional inward turning inlets. Acta Aerodynamica Sinica. 40, 77–83 (2022) (in Chinese). https://doi.org/10.7638/kqdlxxb-2021.0375
9. He, X., Zhou, Z., Mao, P., Le, J.: Design and experimental study of osculating inward turning cone waverider/inlet (OICWI). Journal of Experiments in Fluid Mechanics. 28, 39–44 (2014) (in Chinese). https://doi.org/10.11729/syltlx20120176

10. 10. Zhao, Z.-T., Huang, W., Yan, L., Zhang, T.-T., Li, S.-B., Wei, F.: Low speed aerodynamic performance analysis of vortex lift waveriders with a wide-speed range. Acta Astronautica. 161, 209–221 (2019). https://doi.org/10.1016/j.actaastro.2019.05.029
11. Wang Q.-W., Liu J.: The Osculating Method of The Dual Waverider Geometry Generation, National University of Defense Technology, (2015)(in Chinese).
12. Zhao, Z.-T., Huang, W., Li, S.-B., Zhang, T.-T., Yan, L.: Variable Mach number design approach for a parallel waverider with a wide-speed range based on the osculating cone theory. Acta Astronautica. 147, 163–174 (2018). https://doi.org/10.1016/j.actaastro.2018.04.008
13. Zhao, Z., Huang, W., Jin, H., Wang, H., Dong, Y.: Effects of Mach number discrete method on shape and aerodynamic performance of osculating cone variable Mach number waverider. Acta Aeronautica et Astronautica Sinica. 41, (2020) (in Chinese). https://doi.org/10.7527/S1000-6893.2020.24074
14. He, X.-Z., Zhou, Z., Ni, H.-L.: Integrated design methods and performance analyses of osculating inward turning cone Waverider Forebody Inlet(OICWI). Journal of Propulsion Technology. 33, 510–515 (2012) (in Chinese).
15. Li, Y., Zheng, X., Shi, C., You, Y.C.: Integration of inward-turning inlet with airframe based on dual-waverider concept. Aerospace Science and Technology. 107, (2020). https://doi.org/10.1016/j.ast.2020.106266
16. Li, Y., Zhou, X., Zhu, C., You, Y.: Integration design and analysis for curved conical forebody and three-dimensional inward turning inlet. Journal of Aerospace Power. 33, 87–96 (2018) (in Chinese). https://doi.org/10.13224/j.cnki.jasp.2018.01.011
17. Qiao, W., Yu, A., Yang, D., Le, J.: Integration design of inward-turning inlets based on forebody shock wave. Acta Aeronautica et Astronautica Sinica. 39, (2018) (in Chinese). https://doi.org/10.7527/S1000-6893.2018.22078
18. QIAO, W., YU, A., GAO, W., WANG, W.: Design method with controllable velocity direction at throat for inward-turning inlets. Chinese Journal of Aeronautics. 32, 1403–1415 (2019). https://doi.org/10.1016/j.cja.2019.04.012
19. Sobieczky, H., Dougherty, F., Jones, K.: Hypersonic Waverider Design from Given Shock Waves. (1990)
20. Zhou, H., Jin, Z., Ge, N.: Design method for non-axisymmetric generalized internal conical flowfield based on double 3D curved shock waves. Aerospace Science and Technology. 105, (2020). https://doi.org/10.1016/j.ast.2020.105971
21. Qiao, W.-Y., Yu, A.-Y., Wang, Y.-H.: An Inverse Design Method for Non-uniform Flow Inlet with a Given Shock Wave. Acta Mathematicae Applicatae Sinica. 35, 287–304 (2019). https://doi.org/10.1007/s10255-019-0819-5
22. Wu, Z., Xu, Y., Wang, W., Hu, R.: Review of shock wave detection method in CFD post-processing. Chinese Journal of Aeronautics. 26, 501–513 (2013). https://doi.org/10.1016/j.cja.2013.05.001
23. Wei M.-Q., He X.-Y., Wu M., Guo Y.-W., Tan H.-J.: Geometric Design of B-Spline Aircraft Inlet Based on Curvature Guidance. Journal of Computer-Aided Design & Computer Graphics. 35, 1822–1832(2023)(in Chinese).
24. Xiang, X., Babinsky, H.: Corner effects for oblique shock wave/turbulent boundary layer interactions in rectangular channels. J. Fluid Mech. 862, 1060–1083 (2019). https://doi.org/10.1017/jfm.2018.983
25. Post, F.H., Vrolijk, B., Hauser, H., Laramee, R.S., Doleisch, H.: The State of the Art in Flow Visualisation: Feature Extraction and Tracking. Computer Graphics Forum. 22, 775–792 (2003). https://doi.org/10.1111/j.1467-8659.2003.00723.x
26. Wang, Z., Xin, X., Chen, R., Huang, R., Kong, C., Chang, J.: Development and evolution

mechanism of streamwise vortex in an inward-turning inlet. Proceedings of the Institution of Mechanical Engineers, Part G: Journal of Aerospace Engineering. 237, 3413–3434 (2023). https://doi.org/10.1177/09544100231194882

27. Holden, M.S., Wadhams, T.P., MacLean, M.: Experimental studies to examine Viscous/Inviscid interactions and flow chemistry effects of hypersonic vehicle performance. Presented at the (2005)